Version of Record: https://www.sciencedirect.com/science/article/pii/S027861251930041X
Manuscript_b1d426c52092934fcd0491ea0b5612cb

In-situ monitoring of electrohydrodynamic inkjet printing via scalar diffraction for printed droplets

Xiao Zhang[a,1], Benjamin Lies[a,1], Hao Lyu[a,b*], Hantang Qin[a,*]

[a] *Industrial and Manufacturing Systems Engineering Department, Iowa State University, Ames, Iowa, 50011, USA*
[b] *College of Mathematics and Physics, Qingdao University of Science & Technology, Qingdao, Shandong,266061, China*
[1] *Co-first Author.*

* Corresponding author. Hantang Qin, Tel.: +1-515-294-1248. *E-mail:* qin@iastate.edu
Hao Lyu, *E-mail:* lvhao@qust.edu.cn

Abstract

Electrohydrodynamic inkjet (e-jet) printing is a technique which utilizes electrical forces to generate droplets in micro/nano scale using conductive inks. Currently, there is no procedure in place to measure the printed patterns without taking the sample away from the printer setup. Removal of the substrate from the printing stage during the e-jet printing process prevents any additional work from being performed on the sample. We investigated the application of scalar diffraction for the *in-situ* measurement and digital reconstruction of opaque material printed on transparent substrates. Measurement and characterization of the printed material can be achieved *in-situ* to alter printing condition in process for quality assurance. In order to accomplish the sample reconstruction, a digital recording of a scalar diffraction pattern in the image plane was employed in this paper with a magnification of 5x with the help of a combination of lenses. The reconstructed images were then compared to images captured by an offline high-resolution microscope. The results indicated a submicron accuracy of the feature radii and the locations of feature centers. In addition to the quantitative measurements, this method also allows for the operator to view the overall form of the printed patterns. Our findings demonstrate an effective approach for *in-situ* monitoring of e-jet printing and printed patterns, which could pave the way for the industrial application in printing testing field.

Keywords: electrohydrodynamic; inkjet printing; in-situ monitoring; scalar diffraction.

1. INTRODUCTION

As the need for flexible electronics grows rapidly, the fabrication of small electronic components in micro and nano scale has been significantly necessary [1]. Traditionally, etching and masks were used to fabricate these structures. These methods face drawbacks, however, namely poor customizability and high cost, which are difficult to overcome in order to achieve the high-resolution pattern [2]. Moreover, the requirement of a clean room environment further increases the difficulty of quick prototyping for electronic components and devices. Electrohydrodynamic jet (e-jet) printing is an emerging method for the fabrication of micro/nano structures in electronics and optical fields. This technique has the ability to print high-resolution patterns down to sub-micron with stable droplet generation in addition to fast fabrication for electronics

(e.g., sensors) [3]. With further development of the e-jet printing technique, advanced fabrication of electronics became possible. Dong [4] fabricated self-recoverable and stretchable electronics by e-jet printing technique and further demonstrated the high-resolution capability of manufacturing these flexible electronics by finite element method, which could be the foundation of closed-loop control system if advanced monitoring system could be developed. Rogers [5] used e-jet printing to form patterns of quantum dots for light-emitting diodes. Our group [6] applied the e-jet printing technique to fabricate capacitive touch sensors and achieve sub-20 µm conductive pattern on a flexible insulating substrate. For better control of the e-jet printing process, many methods were proposed to improve the printing quality further. Dong [7-9] used modulated ac-pulse voltage to minimize the residual charge issue and overcame the long-predicted charge accumulation problem on highly insulating substrates. With better voltage control strategy, Mishara [10] demonstrated high-speed printing capability at 1 kHz with 3-5 µm droplet size for an aqueous ink and 1-2 µm for a photocurable polymer ink. High-speed e-jet printing method had the additional advantage of reducing the line-pattern width. Phung [11] reported that the pattern width could be reduced from 20 µm to 4 µm by increasing the speed from 10 mm/s to 50mm/s.

In order to improve reliability and quality control of e-jet printing process, many approaches were explored to investigate the influence of printing and material parameters. Lee [12] investigated the effect of viscoelasticity of typical ink on Taylor cone formation using a two-model system. Han [13] applied the e-jet printing process for phase-change wax material; both experiment result and FEA models demonstrate agreement with each other. Ink characteristics played a large part in the final quality of printed patterns, and one such ink characteristic was the solvent used. Je [14] used silver nanoink for printing, which contained a low boiling point solvent, and the results were dots and lines with superior quality. However, it was difficult to monitor the results of these altered printing parameters. Many researchers focused on the image processing process to instruct the printing process such as Gardner [15] reported the operation of optical coherence tomography in a selective laser sintering system to monitor the surface feature of the printed part. Similar research has been done by Grasso [16], a method was proposed for detection and recognition of spatial defects during the selective laser melting process, but challenges remain under different frame rates at the same experimental setup. During the ink-jet printing process of Liquid Metal Inkjet Printing (LMIP), Wang [17] solved the uncertain factors by using vision-based closed-loop control system which achieved stable jetting behavior; however, the droplet sizes were limited to a few hundred microns. Imani [18] proposed image-based method to collect nonlinearity, irregularity during the manufacturing process, which link the process parameters with in-process images. Wang [19] applied in-situ droplet inspection based on image analysis for liquid metal jet 3D printing, but not for printed parts. Liu [20] developed an image-based closed-loop system to diagnosis the fused filament fabrication system with captured images and provided the automatic adjustment of the parameters to detect the defects. The system worked well for continuous printing (filament) but not for discrete droplet-based printing. In previous works, we [21] used machine vision to enable real-time monitoring of the e-jet printing process and the implementation of a feedback control system to achieve a higher quality pattern. The quality of the manufacturing process could be influenced by particle

distribution, Kam [22] analyzed the images of particle distribution to provide general guidelines to the manufacturing process in nanomanufacturing and biomanufacturing. It was proved significant that quality assurance via monitoring should be ensured during manufacturing processes. A similar machine vision system was used by Lee [23], who applied a vision algorithm to enable *in-situ* measurement of the e-jet printing process. Both of these vision processes monitored the Taylor cone formation, but they did not show the pattern printed on the substrate in real-time.

Currently, measurements of printed results are usually performed offline via an optical microscope or other similar metrology methods, which results in the removal of the substrate from the printing platform. Once the substrate has been removed, additional printing is impossible as realignment is difficult and most time is not feasible. An alternative new method for *in-situ* monitoring and characterization of such printed droplets is needed. Inkjet-based printing is a droplet driven process. The measurement of dot patterns (formed by droplets) is the key step before the realization of printing high quality patterns. Successful dot patterns could be used for micro/nano array patterning, and line patterns could contribute to the manufacture of devices such as wearable sensors. Laser diffraction system is flexible for measurement in various environments and robust for *in-situ* characterization. In this contribution, we demonstrated an approach using scalar diffraction for the *in-situ* measurement and digital reconstruction of e-jet printing. A digital recording of a scalar diffraction pattern in the image plane was employed to evaluate the printed results in process. This approach could open a new way for *in-situ* monitoring and characterization of e-jet printing.

2. FABRICATION SETUP: E-JET PRINTING PROCESS

The experimental setup of e-jet printing was shown in Fig. 1a. A commercial silver nanoink was used as the printing material for this experiment. A three-axis nano-positioning stage was used for the movement of the printer head and substrate. During the printing, the movement in x and y direction was programmed in the horizontal plane for printing on the substrate. The z direction was programmed to obtain a desired standoff distance from the nozzle tip to the substrate. The positional resolution along the x and y direction was 50 nm, and the speed of lateral directional movement could vary from 0.001 mm/s to 20 mm/s. The substrate used as the printing platform was transparent (e.g., glass slides or PET films) and the standoff distance was set to 20 µm. A high electric potential was applied between the nozzle and substrate, with the voltage ranging between 500V to 1000V. The positive and negative electrodes of the voltage supplier were connected with the nozzle and the substrate, respectively. The diameter of the nozzle varied between 2 to 30 µm. With such small sizes, the surface tension of ink prevented droplet formation at the tip of the nozzle without a voltage supply. The electrical force drove the silver nanoink out of the nozzle onto the substrate and served as the primary force for stable jetting the material. A camera was used to monitor the region between the nozzle and the substrate. After the settlement of the nozzle on the system, the positive and negative electrodes of the voltage supply were connected with the nozzle and the substrate, respectively. Via control of process parameters (e.g., voltages, plotting speed, etc.), different sizes of silver droplets, dots, and lines were achieved, as shown in Fig. 1b.

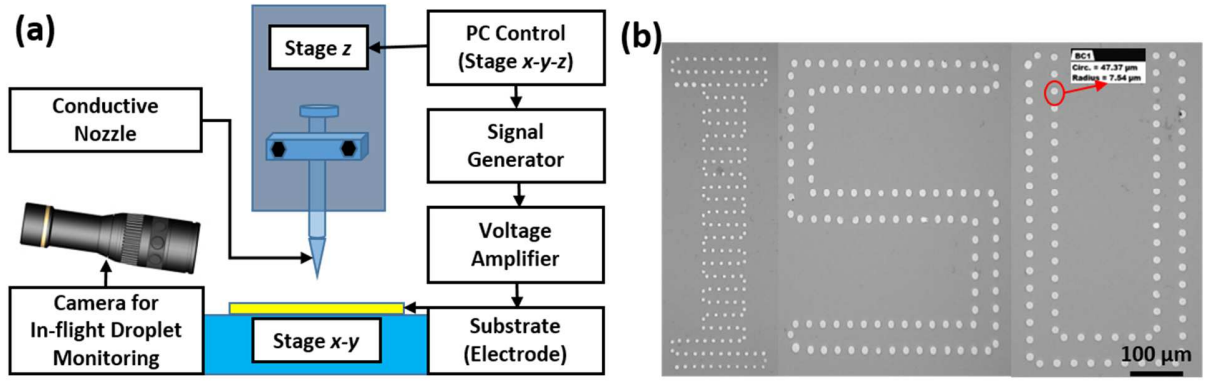

Fig. 1: (a) Schematic of e-jet printing, and (b) printed droplet patterns

In a traditional setup of e-jet printing, the camera shown in Fig. 1a was used to observe the region between the nozzle and the printing substrate, and to monitor the in-flight droplet behavior. The resolution of such optical zoom lens and camera could be as high as 2 µm with associated cost around $4000. However, this *in-situ* setup could not observe the pattern being printed. Aligning additional zoom lens system on the *z* stage increased extra load and reduced control resolution of the *z*-axis. This means that the operator could only predict what the printed pattern would look like based on the printing parameters established beforehand using a traditional setup in Fig. 1a. These parameters included voltage, ink characteristics, standoff distance, translation speed, etc. Currently, the method to characterize the printed pattern was to remove the substrate from the printing stage and to conduct metrology offline using microscopy (SEM or optical). Removal from the stage eliminated the possibility for any additional future printing as there was no longer any point of reference and the small scale of the printing made realignment very difficult. Without an effective approach to recognize printed patterns *in-situ* or establish a point of reference for future alignment, quality control of e-jet printing would likely to remain difficult. In this paper, a scalar diffraction vision system was developed to resolve the challenge.

3. SCALAR DIFFRACTION VISION SYSTEM

The following scalar diffraction system was proposed to solve the challenges mentioned in previous sections regarding quality assurance and feature recognition for e-jet printing. Fig. 2a demonstrated the optical equipment location as it would relate to the e-jet printing setup and Fig. 2b showed the specifics of the components of the optical system setup.

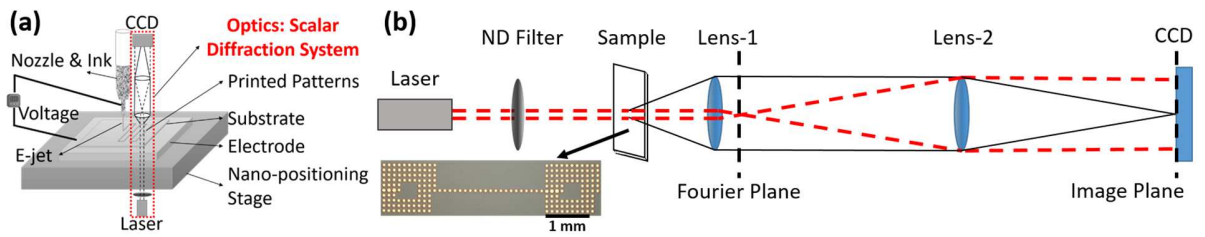

Fig. 2 : (a) Location of scalar diffraction system in e-jet printing setup, and (b) a schematic of the optical components for scalar diffraction: Laser, Step variable neutral density filter (ND), Sample, Lens-1, Lens-2, and Charge Coupled Device (CCD).

The laser as a light source used in this experiment was a 2 mW HeNe laser (wavelength 632 nm). The light then passed through a step neutral density (ND) filter. The magnitude of this filter was set such that the light incident on the CCD did not saturate the camera in order to preserve as much information as possible. The sample used in this experiment was silver nanoink printed on a transparent substrate via e-jet printing. The ink pattern was on the side opposite the incident light. Nemoto investigated the propagation of a Gaussian beam when passing through a dielectric material and determined that the waist size of the beam was unchanged when the light was normal to the surface of the substrate [24]. Some of the incident beam was then diffracted by the sample pattern, and the unscattered light passed through the transparent substrate (reference beam). The light diffracted due to the sample was then collimated by Lens-1 while also focusing the reference beam such that it could be represented by a single point in the Fourier plane. The Fourier plane was located behind Lens-1 at a distance equal to the focal length of Lens-1. The second lens, Lens-2, focused the collimated diffraction pattern resulting in the formation of the original image multiplied by the magnification that resulted from the objective lens system.

In this optical configuration, the digital sensor (e.g., charge coupled device CCD) could record an intensity pattern in either the Fourier plane or the image plane. Each of these planes had unique characteristics. The Fourier plane was observed after the incident light had been diffracted by the sample and the resulting pattern was observed in the far field. In order to satisfy this far field condition, the diffraction pattern resulting from the light incident to the sample was collimated by a lens. This collimated pattern effectively described the pattern at infinity. This far-field pattern was typically referred to as the Fraunhofer regime, which was often described in terms of frequency. An example of a pattern recorded in the Fourier plane was shown in Fig. 3a. The image plane contained the reconstruction of the target sample in the spatial domain. An example of a pattern recorded in the image plane was shown in Fig. 3b.

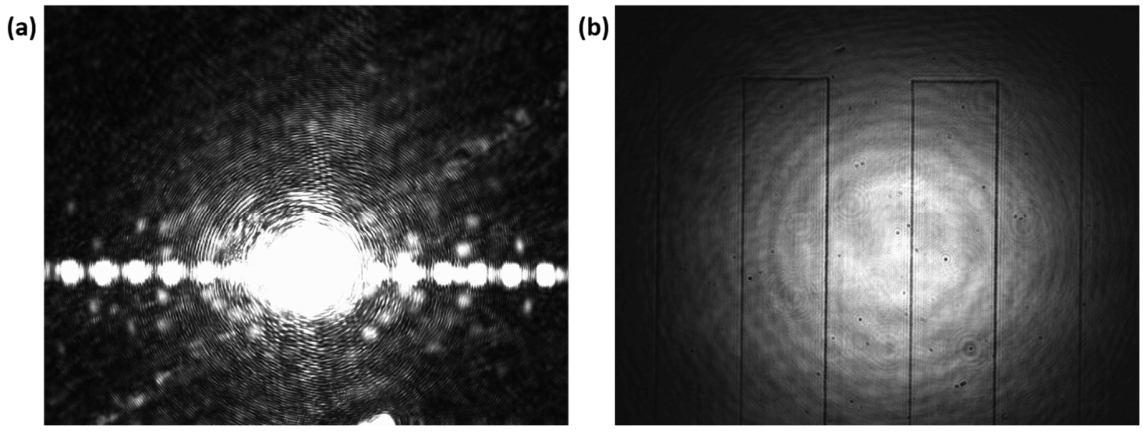

Fig. 3: Intensity distribution resulting from the printed pattern in the (a) Fourier plane and (b) image plane.

The Fraunhofer diffraction was described as the product of multiple approximations made in optics. Initially, the Huygens-Fresnel principle [25] was used to describe the diffraction of an object through the summation of small wavelets around the contour of an object or through an aperture. Later, the Fresnel-Kirchhoff integral theorem [26] expanded upon this theory through the implementation of Greens theorems [27]. The resulting equations were then approximated and categorized into two fields, Fresnel (near field) and Fraunhofer (far field) diffraction [28, 29]. The integrals associated with Fresnel diffraction were computationally challenging to solve outside of several known configurations. Thus, the most straightforward approximation (computationally) was the Fraunhofer approximation, which utilized the Fourier transform to solve mostly due to the implementation of the Fast Fourier Transform (FFT) [30].

In the Fourier plane, the intensity distribution was a continuous function describing the frequency domain, but the device used for digital recording was discrete, which indicated that an insufficient sampling rate could result in aliasing of the data. In order to accurately recreate the continuous signal, the Nyquist-Shannon Sampling Theorem [31] should be implemented, which described the resolution restrictions due to predefined sensor parameters and the bandwidth limitations of the system. In addition to resolution limits imposed by discrete sampling, the intensity distribution in the Fourier plane had a couple of unwanted components. These components were the twin image and zero order image. There have been many methods proposed to isolate and differentiate the useful information from the twin and zero-order images. These methods required additional processing time however and should be avoided if possible.

The alternative to the Fourier plane was the image plane. The resolution of the image plane was not restricted by the Nyquist-Shannon Theorem as another lens was added which acted as a continuous inverse Fourier transform [32]. This resulted in an image of the sample plane multiplied by a magnification factor determined by the combination of lenses acting as the objective. As a result, recording in the image plane removed the need to experimentally or computationally remove the twin and zero-order image. The only calculations needed to interpret the image plane were the magnification due to the objective lens combination and the conversion from the image plane to the sample plane. The image resulting from the first lens was then used as the object for the second lens. The magnification of each lens depended on the distance at which the object was being observed.

The resolution in the image plane was determined as a function of effective magnification and the discrete sample sizing of the camera. The resolution of the camera and FOV regarding the sample plane could then be determined. There were several factors which may limit resolution in the system. The diffraction of light as it passed through a lens was an unavoidable problem. This resolution limit was typically calculated and used as an ideal case. In our study, the objective lens had a numerical aperture of 1/9.8. This resulted in a resolution limit of 3.096 μm in the sample plane. The camera pixel corresponded to an area of 0.92 μm in the sample plane. As a result, the resolution limitation was due to the diffraction. A resolution of 3 μm was small in comparison to the feature sizes of the sample. In this case, the limiting factor would be the camera itself.

4. IMAGE PROCESSING

E-jet printing could generate droplet and dot patterns on flexible and transparent substrates as shown in Fig. 1b. In this study, in order to utilize scalar diffraction system for quality assurance of e-jet printing, we fabricated the patterns with certain common defects (e.g., non-circularity, line coalescence, droplets connection, etc.). Imaging processing algorithms were developed to perform feature recognition and quality control.

3.1. Background Analysis

In the image plane, the unscattered light was magnified onto the camera in a Gaussian shaped intensity pattern. This Gaussian pattern was constant among all of the images, so it was essential to isolate and remove this pattern. Several images were taken when there was no printed silver dots on the substrate. The average between these images was used in order to reduce the noise caused by any dust that could be on the transparent substrate. The average was found using Equation 5,

$$\mathrm{B(x,y)} = \frac{\sum_{\mathrm{i=0}}^{\mathrm{n}} \mathrm{b_i(x,y)}}{\mathrm{n}} \tag{5}$$

where $B(x,y)$ represented the average pixel intensity for a given pixel. Each individual background image was represented by b_i where the number of images averaged was n. There were several perturbations which were consistent throughout all of the background images which did not require to be removed as they would remain in the sample image as well. In Fig. 4, a reducible disturbance has been circled in red for both images.

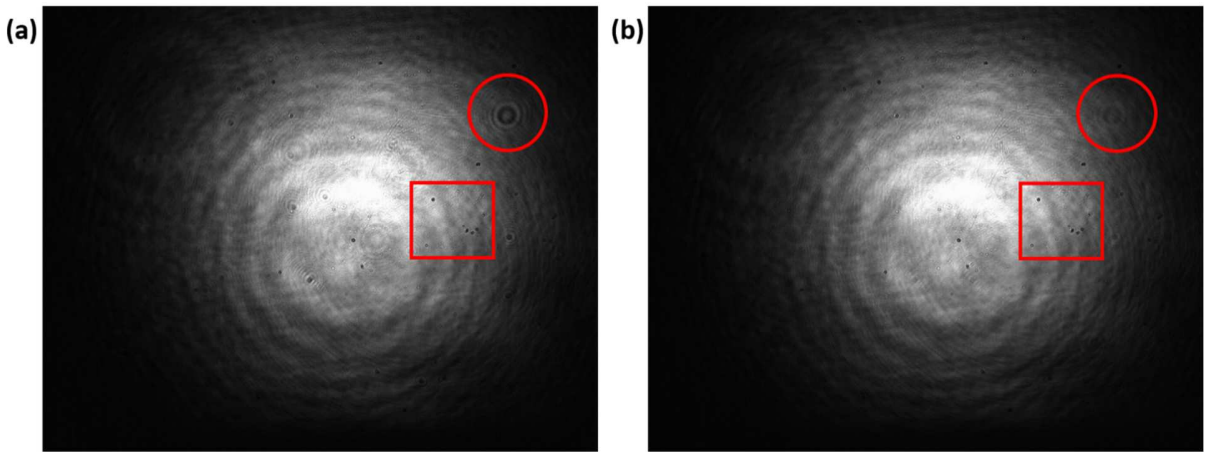

Fig. 4: (a) Singular background images with a unique disturbance (red circle) and several consistent disturbances (red square), and (b) average of several background images.

This was an example of how the intensity of the noise, which was inconsistent in the images (unique), was reduced. The square indicated several dots which were constant among all of the background images taken. This was dust on a lens or the camera itself which would be consistent in every image, thus remaining during the average procedure. The sample image was then

subtracted from the average background image. The sample produced a darker pattern in the shape of the sample. Thus any negative values resulting from the subtraction could be set to '0'. This reduced noise as well as errors caused by an imperfect background image. The result was a sample pattern in greyscale without the reference beam. This was shown in Fig. 5a. The mathematical representation of this subtractive process was depicted in Equation 6.

$$D(x,y) = \max(B(x,y) - S(x,y), 0) \tag{6}$$

where $S(x,y)$ represented the individual pixels resulting from the light incident on the sample. This greyscale image contained sample information as well as some additional noise which resulted from the light passing through the finite lenses. The differentiation between these two categories was completed through binarization and filtering.

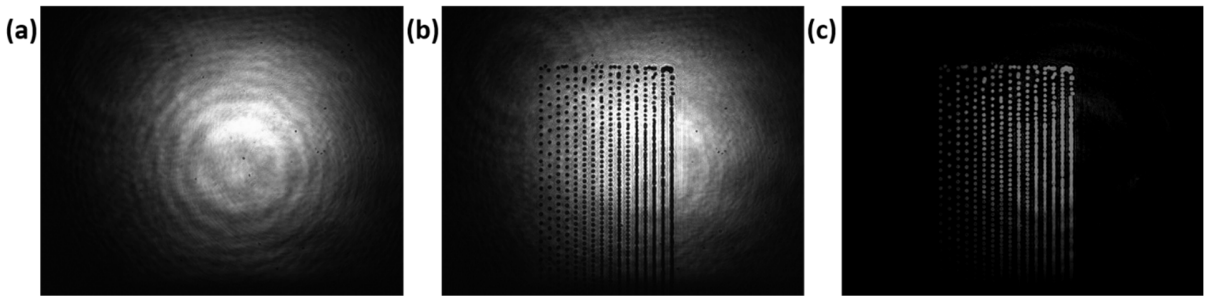

Fig. 5: (a) The average background image described by Equation 1, (b) the sample image, and (c) the result of the subtractive process described by Equation 2.

3.2. Binarization and Filtering

This magnified sample image contained locational and dimensional information for identification of reference point and evaluation of printing quality. In order to achieve real-time image processing, a binarization technique was used to convert the image from a greyscale into a black and white. The black represented the background while the white represented the pattern printed on the substrate. The binarization technique used in this experiment utilized local adaptive thresholding [33], which created several smaller windows inside the main image. Each neighborhood was approximately one eighth the size of the original image. In our algorithms, the mean of the neighborhood intensities was determined, and a sensitivity value was assigned by the user. The threshold for each neighborhood was a percentage of the mean value based on the sensitivity. The higher the sensitivity, the lower the threshold value resulting in more foreground pixels being identified. All of the intensity values of the pixels in the neighborhood were compared to this threshold. The greyscale image was then converted to black and white based on this threshold value. The value chosen for sensitivity was significant. For an image shown in Fig. 5c, a sensitivity that was too low could result in the loss of sample information (Fig. 5a), and a sensitivity that was too high could result in amplification of noise or saturation of the sample (Fig. 6b). It was also observed that by increasing the number of pixels above the threshold, the size of a feature varied slightly.

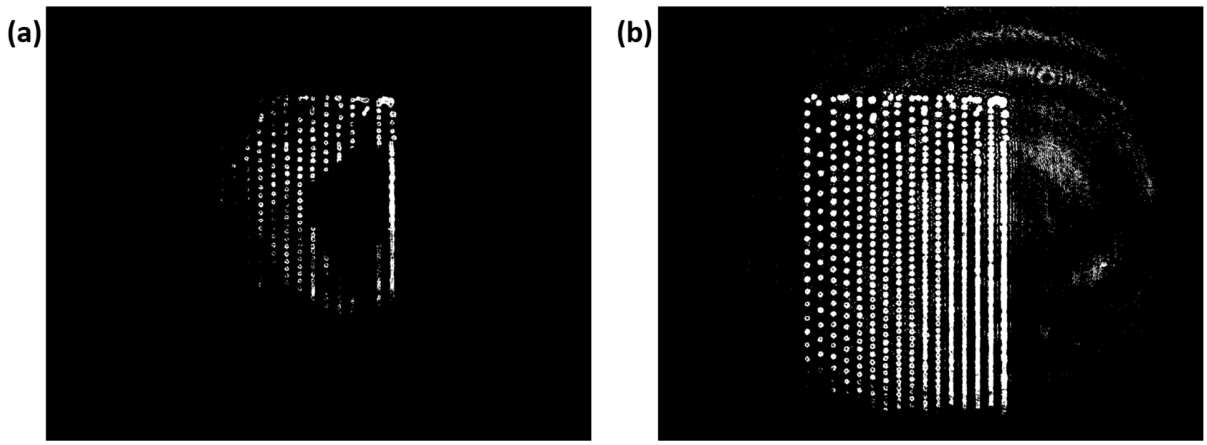

Fig. 6: (a) Image binarization using a low sensitivity (0.05, assigned by the user) resulting in information loss, and (b) a high sensitivity (0.55) resulting in the amplification of noise.

In order to maintain information without the inclusion of too much noise, a sensitivity somewhere in the middle must be chosen. Some noise could still be present, however, in order to remove the noise, a median filter was applied. This filter was able to remove speckle noise and to contract some features. The filtering approach in combination with the selection of the sensitivity could ensure that measured feature size was consistent. It was important to note that a median filter also had the capability to fill in holes and connect features that were one or two pixels away from each other. These influences were dependent on the filter size however and could be minimized by using a small filter size.

3.3. Cropping and Combining

The data from image plane could be binarized, but it has been observed that the areas with low contrast between the sample images and the background were not always reconstructed correctly, which limited the smart feature recognition of the system. In order to combat this, a region of interest (ROI) case study was established. The ROI was positioned over the area with the most significant contrast, the center of the Gaussian light. The ROI did not move as the background light remains the same while the sample was moving during printing. In this work, the ROI has been established to be a 400 x 400 pixel region. The size was determined in order to maintain the high quality of information as well as a large physical area covered. The ROI of the sample that was used for further investigation was shown in Fig. 7. As mentioned in the previous section, the patterns were designed to reflect potential defects and to present different printing conditions.

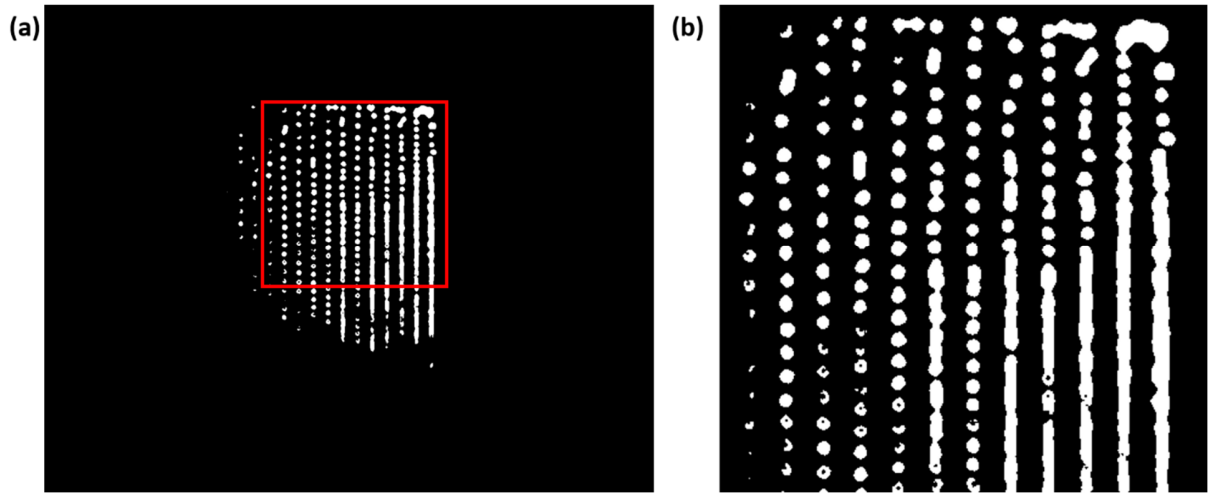

Fig. 7: (a) The full binarized image with the ROI identified, and (b) a full view of the ROI.

Once the region of interest has been established, several ROI could be combined in order to reconstruct the entire image. Currently, this was achieved through feature matching. An example of a combination of two ROI was shown in Fig. 8 in comparison to the same pattern under a digital microscope. As previously mentioned in the binarization and filter section, it could be seen that when the features were close to each other, some features were combined. This was caused by the selection of the binarization sensitivity or the work of the median filter.

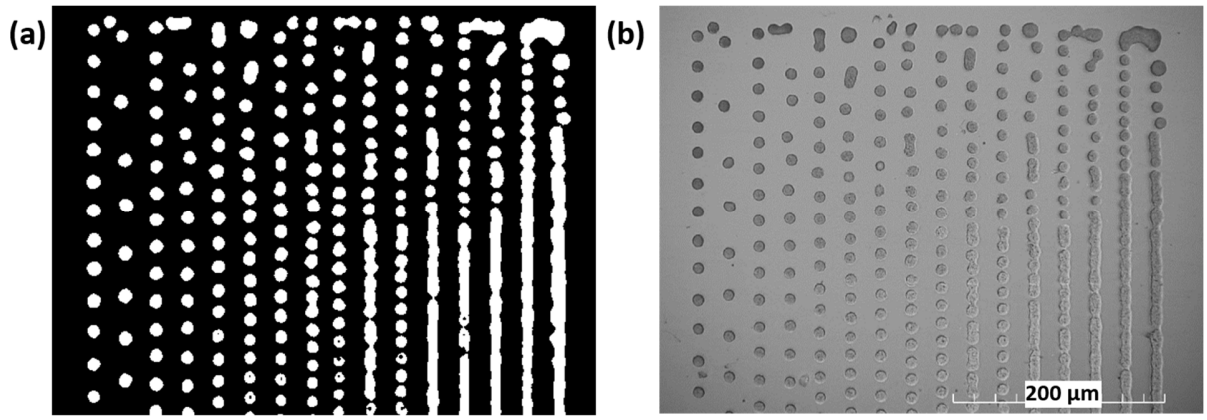

Fig. 8: (a) Combination of two ROI with its counterpart captured by (b) the microscope.

3.4. Circle Finding

After image reconstruction of the sample, the reconstructed images could then be analyzed to identify key features. The specific sample used in this study aimed to create a dot pattern so the feature identification approach will identify circles via circular "Hough" transform [34]. The method utilized the boundaries of each connected body. A circle was then applied to those candidates. These circles corresponded to a cone in the 3D Hough parameter space. The theory for the space could be represented as:

$$(x-a)^2+(y-b)^2=r^2 \tag{7}$$

where (a,b) represented the circle center, and r represented the radius. The candidate pixels were represented by (x,y). The intersections of the resulting cones in the Hough space were collected in an accumulator matrix. The area was determined by the accumulator matrix which counted the intersections. From this matrix, the most suitable circle parameters were determined (a,b,r). This approach also required a sensitivity threshold that must be set by the user in addition to a radius range. With regards to the sensitivity, too low a sensitivity and the program would not be able to pick up a feature unless it was a near perfect circle, and too high a sensitivity and it would show false alarms (FA). An FA was determined to be anything that was identified as a circle by the program which was not determined by the operator to be a circle, typically when multiple droplets were deposited too close resulting in one large figure. The limitation was due to the unique capability of a circular Hough transform which was the ability to find circles that were partially obscured by other objects or features. Examples of several sensitivity values were demonstrated in Fig. 9.

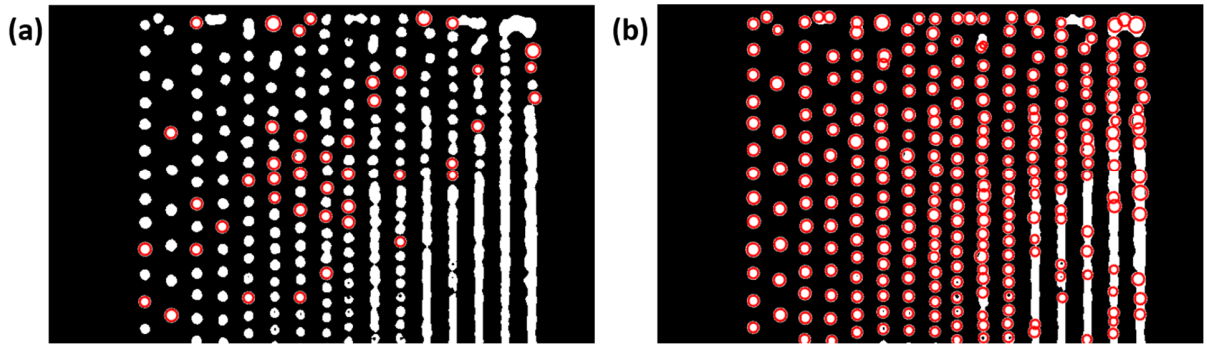

Fig. 9: The images with user defined circle sensitivity which was (a) too low, and (b) too high.

Once a circle has been identified, the radius and location of the circle were recorded. The accuracy, precision, and reliability of these location and size measurements would be compared with those measured by an optical microscope in the following section. In addition to the radius and location of the circle size, image processing could delete circles that overlapped. Overlapping circles can be seen in the top right corner of Fig. 9b. Depending on the preference of the operator, these could be removed in order to reduce the number of FA. Via the analysis of printed dots and image processing, the dot quality was easy to estimate, which could give direct guidance and feedback of printing parameter optimization.

5. RESULTS AND DISCUSSIONS

In the previous section, the selection procedure for the binarization sensitivity, median filter size, and the circle finding sensitivity have been discussed. These constants corresponded to the imbinarize(), medfilt2(), and imcirclefind() functions in Matlab. A range was set for each of these constants, and then each combination was processed and characterized. The binarization constant ranged from 0.15 to 0.25 in increments of 0.01. A smaller binarization constant resulted in the loss of dots and a larger constant resulted in additional noise and inflation of the dots (as

shown in Fig. 6a-b). The median filter size ranged from 3 to 6 pixels in increments of 1. A smaller filter size resulted in poor noise reduction, and the larger filter size was more likely to combine dots and removed smaller dots entirely. The last constant, the circle finding sensitivity, ranged from 0.85 to 0.95 in increments of 0.01. Sensitivities smaller than 0.85 resulted in many "misses" and sensitivities higher than 0.95 resulted in a larger number of FA. In total, 484 combinations were tested. From these 484 variations, any combination which missed a dot was removed. In addition, the minimum circle sensitivity was used in order to reduce unnecessary false alarms. The result of these constraints were 18 different combinations as shown in Table 1.

Table 1. Different combinations of constants in imaging processing to test the scalar diffraction approach for identification of printed dot patterns.

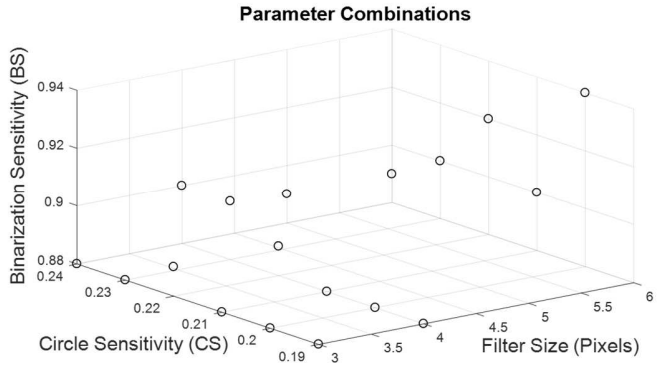

Filter Size	Binarization Constant	Circle Sensitivity	Filter Size	Binarization Constant	Circle Sensitivity
3	0.19	0.88	4	0.22	0.89
4	0.19	0.88	6	0.22	0.92
3	0.2	0.88	3	0.23	0.88
4	0.2	0.88	4	0.23	0.9
6	0.2	0.94	6	0.23	0.9
3	0.21	0.88	3	0.24	0.88
4	0.21	0.88	4	0.24	0.9
6	0.21	0.9	5	0.24	0.89
3	0.22	0.89	6	0.24	0.89

Utilizing the combinations in Table 1, size distributions were created which represented the size distribution of the dots. These image processing size distributions (IPSD) were then compared with the microscope measured size distributions (MMSD).

When comparing the IPSD and the MMSD, it was noted that the distributions appeared relatively normal, as shown in the probability density function in Fig. 10a. Thus, modeling them under the assumption that they were normally distributed that allowed for the computation of the mean and the standard deviation, both of which could be used to characterize the data as shown in Fig. 10b.

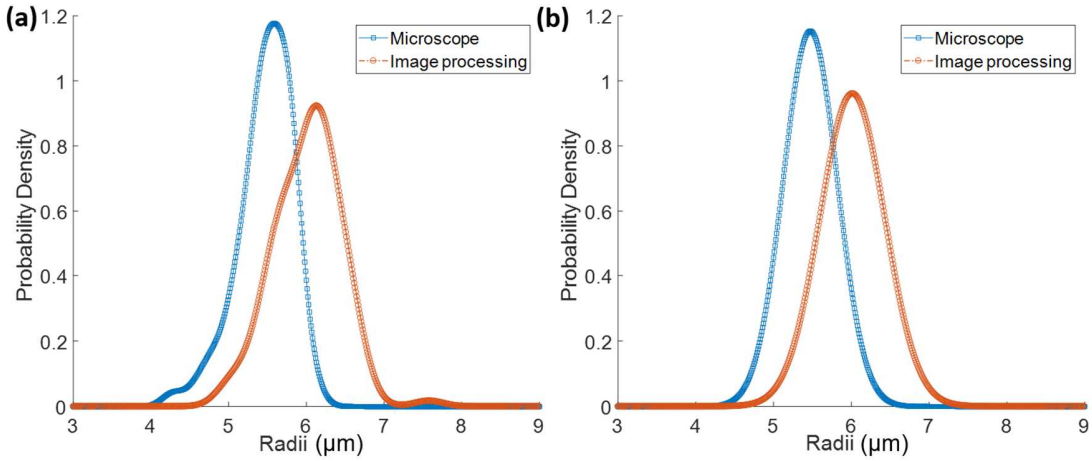

Fig. 10: (a) Radii comparison between the microscope and image processing algorithm, and (b) after normalization.

In addition, the number of false alarms could be easily determined as the remaining combinations have no "misses" and the number of "hits" was known. In the study, the defining characteristics were the absolute difference between the IPSD μ_1 and the MMSD μ_2 (denoted $\Delta\mu$), the absolute difference between the IPSD σ_1 and the MMSD σ_2 (denoted $\Delta\sigma$), and the number of false alarms. Each of these 18 combinations was then sorted 1-18 for each of these defining characteristics. The lower values being number 1, higher values being 18. Weight was given to each combination. The weight of each characteristic was subject to change depending on the needs of the operator and specific applications. As one example, Table 2 showed the results of an even weight applied to the $\Delta\sigma$, $\Delta\mu$ and the number of 'false alarms". The performance of each set of image processing parameters was then ranked for each sample group.

Table 2. Results of an even weight applied to the $\Delta\sigma$, $\Delta\mu$ and the number of "false alarms" for optimization of coefficients and constants.

Filter Size	Binarization Constant	Circle Sensitivity	Group 1	Group 2	Group 3	Group 4	Group 5	Group 6	**Total**
5	0.24	0.89	7	1	5	2	1	6	22
6	0.24	0.89	3	2	4	6	3	5	23
4	0.20	0.88	2	4	8	6	2	4	26
4	0.19	0.88	8	3	11	1	4	1	28
3	0.19	0.88	11	10	2	1	4	1	29
6	0.21	0.90	10	6	3	4	5	5	33
3	0.20	0.88	5	14	2	3	9	3	36
6	0.23	0.90	12	5	6	7	6	2	38
4	0.21	0.88	1	9	13	5	5	8	41
6	0.22	0.92	13	11	1	8	4	8	45
3	0.21	0.88	9	8	7	7	8	7	46
6	0.20	0.94	13	12	10	7	7	7	56
3	0.23	0.88	6	15	9	9	9	12	60
4	0.22	0.89	15	7	14	11	6	10	63
3	0.22	0.89	11	16	12	10	11	8	68
3	0.24	0.88	4	18	15	11	12	11	71
4	0.24	0.90	14	17	15	9	10	9	74
4	0.23	0.90	16	13	14	11	10	12	76

There were six different groupings of dots that were observed in this experiment. The first group was shown in the image processing section and can be entirely seen in Fig. 9. The remaining five groups utilized the same image processing routine using the 18 combinations of Filter Size, Binarization Constant, and Circle Sensitivity described in Table 1. Each combination of image processing parameters resulted in a $\Delta\mu$ and $\Delta\sigma$ for each of the six dot groups. From these, the average absolute difference in the mean could be calculated and that the standard deviation of this average was computed as well. This average $\Delta\mu$ could then be plotted as a function of the

binarization sensitivity as well as the filter size as shown in Fig. 11a and Fig. 11b respectively. The circle finding sensitivity was excluded as the lowest value resulting in no misses was chosen.

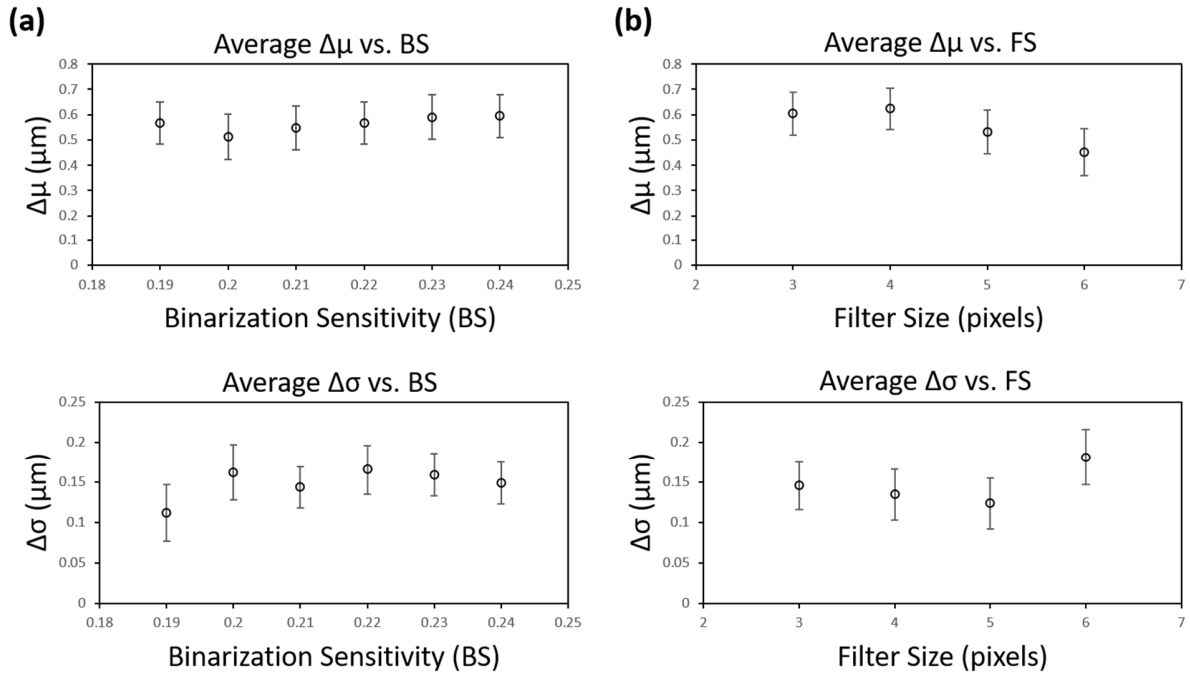

Fig. 11: Average value of (a) binarization sensitivity (BS), and (b) filter size (FS) comparison.

There were several trends in the values shown in Fig. 11. The accuracy and precision were a function of the binarization sensitivity and filter size. The size of these error bars was representative of the standard deviation of the measured Δμ values, of the 18, with regards to binarization sensitivity and filter size respectively. The smaller the quantity, the more accurate the IPSD was to the MMSD. The smaller the error bars, the more consistent and therefore more precise the IPSD was. The results shown in Fig. 11 indicated that there was very little difference in the mean value of this distribution when selecting the binarization constant. When looking strictly at the binarization constant, it was only necessary that the operator chose a value that did not remove desired data points or generate too much noise when selecting the range. The constant should be large enough such that none of the dots were completely removed and small enough such that the noise was not an issue. In our study, a binarization constant of 0.19-0.24 were all sufficient with 0.2 being the most accurate. With regards to precision, 0.19 maintained the most similar standard deviation. When comparing the influence of the filter size, it should be noted that the smaller the filter size, the less accurate the resulting distribution was. When measuring the precision of the system, the largest filter size, 6, had the lowest precision. It was concluded that a filter size of 5 was best for the highest accuracy and precision combination. This filter size had the second highest accuracy and the best precision.

There were several ways that the data could be interpreted. First, the operator may be looking for settings which resulted in a particle size distribution most similar to the measurements given

when measured via a microscope. It represented the most accurate settings or the settings which resulted in the smallest deviation (on average) from the actual distribution, which can be represented by the smallest Δμ values. Second, another measure of the quality of this methodology was the consistency of results between multiple sample areas. The consistency and the grouping of the differences was referred to as the precision of the system, which was represented in this study, as the width of the curve, Δσ. This variability was not necessarily a negative factor as long as it was predictable and could be accounted for. Third, another measure was the number of false alarms present. In the case of feedback control for e-jet printing, false alarm measurement could be misleading and inconsistent systematically. Typically imperfections in this dot printing process were caused by the overlap of multiple dots. This circle detection method, by nature, found well-formed circles and those which were partially obscured, or in this study, overlapped. The operator could not tell if the dots were independent or connected as they were detected the same way in both cases. This made it difficult to draw a conclusion regarding the quality of the reproduction of the IPSD, with respect to the number of FA unless it was reviewed as it did not contain information regarding connectivity. The number of false alarms played a role in the mean and standard deviation of the size distribution; however, so it should not be ignored entirely. As a summary, it was ultimately up to the user and application to determine how each of these factors should be weighed when determining the "best" set of parameters to use for the image processing of scalar diffraction system.

The system has demonstrated good resolution. One of the advantages is the capability to measure sub-30 μm features to within several microns, but the overall performance is dependent on the parameters, not necessarily the system. The system is based on automated image processing with no differences among repeatable tests. We experimented with six different dot patterns and compared those to measurements collected via an optical microscope. The limitation of this system is the requirement of a transparent substrate which may restrict the application of this system in a wider area. Other than that, there are also many advantages. Due to the application of laser source, it has a strong capability to get rid of environmental influences such as distance between object and laser source which enable the flexible setup of this system. The repeatability of this system could be ensured by the single wavelength of a stable laser source which supports the robustness of this laser diffraction system. The study in this paper has advanced the state-of-the-art in-situ¬ monitoring system for micro/nano scale droplet-based inkjet printing. Using the new diagnosis method, the dimension and location of in-flight droplets can be precisely identified, which could be a step towards quality assurance of electrohydrodynamic inkjet printing and construction of complicated cyber-physical micro/nano manufacturing systems.

6. Conclusion

In this paper, a scalar diffraction system was developed for *in-situ* monitoring of printed patterns in e-jet printing. The approach had the capability to calculate the droplet size distribution of a sample without removal from the printing platform with magnification for micro/nano scale detection. The focus of this work is an in-process measurement technique, specifically for e-jet printing on transparent substrates. There are currently no such processes in use, which is an indication that this is the first application of such a system in this field. This work also has the

capability to automate much/all of the inspection process. The measurements made during the image processing were consistent as long as the process parameters were chosen correctly. In addition to the measurements, the scalar diffraction system allowed an easy-setup and low-cost solution for the operator to monitor the quality of the printed sample, which was not currently feasible unless the sample was removed from the workspace and measured offline. The binarization constant should be chosen such that the noise was low while maintaining all of the feature data. The filter size should be chosen to remove the additional noise while maintaining the smaller features and avoiding the combination of dots. The circle finding sensitivity should be chosen such that the lowest number of false alarms were present. Several combinations of these parameters were demonstrated based on our printing setup, and the resulting difference in the size distributions was explained in details.

Our future work will be focusing on a digital twin system for e-jet printing based on metrology. Using the printing quality information as feedback control signals for e-jet printing, the approach could ensure dots were of the correct size for the correct feature and potentially spacing. Another significant contribution was that the approach enables the capability for easy system lineup with a reference dots on substrates when multiple layers of transparent substrates are required for higher dimensional fabrication.

Acknowledgments

This paper is based upon work supported by the U.S. Department of Energy's Office of Energy Efficiency and Renewable Energy (EERE) under the Advanced Manufacturing Office Award Number DE-EE0007897 to Iowa State University. Dr. Lyu is a visiting scholar at Iowa State University (08/15/18-07/31/19), supported by the International Cooperation Program for Excellent Lectures of 2017 by Shandong Province Education Department. Their supports are greatly appreciated.

Declarations of interest:

The patent application of the scalar diffraction system is currently under view at Office of Intellectual Property and Technology Transfer office at Iowa State University for US Patent, and has been patented in National Intellectual Property Administration (CNIPA, Chinese Patent Office, Patent #: 201910207498.1). The authors declare that they have no other known competing financial interests or personal relationships that could have appeared to influence the work reported in this paper.

NOMENCLATURE

ND	step neutral density filter
f	focal length of the lens

d_0	distance from the object to the lens center
d_i	distance from the lens to the resulting image
m_1, m_2, M	effective magnification of lens-1, lens-2, and the system
NA	numerical aperture of objective lens
R	resolution limit
λ	Wavelength of laser
$B(x, y)$	average pixel intensity
$S(x, y)$	individual pixels from light incident
$D(x, y)$	resultant grayscale of sample pattern
FA	false alarms
$IPSD$	image processing size distributions
$MMSD$	microscope measured size distributions
μ, σ	average and standard deviation of distributions

References

[1] Galliker, P., Schneider, J., Eghlidi, H., Kress, S., Sandoghdar, V., and Poulikakos, D., 2012, "Direct printing of nanostructures by electrostatic autofocussing of ink nanodroplets," Nature communications, 3, pp. 890.

[2] Onses, M. S., Sutanto, E., Ferreira, P. M., Alleyne, A. G., and Rogers, J. A., 2015, "Mechanisms, capabilities, and applications of high-resolution electrohydrodynamic jet printing," Small, 11(34), pp. 4237-4266.

[3] Prasetyo, F. D., Yudistira, H. T., Nguyen, V. D., and Byun, D., 2013, "Ag dot morphologies printed using electrohydrodynamic (EHD) jet printing based on a drop-on-demand (DOD) operation," Journal of Micromechanics and Microengineering, 23(9), pp. 095028.

[4] Han Y., and Dong, J., 2018, “Fabrication of self-recoverable flexible and stretchable electronic devices,” Journal of Manufacturing Systems, 48, pp. 24-29.

[5] Kim, B. H., Onses, M. S., Lim, J. B., Nam, S., Oh, N., Kim, H., Yu, K. J., Lee, J. W., Kim, J.H., Kang, S.K., et.al., 2015, "High-resolution patterns of quantum dots formed by electrohydrodynamic jet printing for light-emitting diodes," Nano letters, 15(2), pp. 969-973.

[6] Qin, H., Cai, Y., Dong, J., and Lee, Y.S., 2017, "Direct printing of capacitive touch sensors on flexible substrates by additive e-jet printing with silver nanoinks," Journal of Manufacturing Science and Engineering, 139(3), pp. 031011.

[7] Qin, H., Dong, J., and Lee, Y.S., 2017, "AC-pulse modulated electrohydrodynamic jet printing and electroless copper deposition for conductive microscale patterning on flexible insulating substrates," Robotics and Computer-Integrated Manufacturing, 43, pp. 179-187.

[8] Wei, C., Qin, H., Ramirez-Iglesias, N. A., Chiu, C.P., Lee, Y.S., and Dong, J., 2014, "High-resolution ac-pulse modulated electrohydrodynamic jet printing on highly insulating substrates," Journal of Micromechanics and Microengineering, 24(4), pp. 045010.

[9] Wei, C., Qin, H., Chiu, C.P., Lee, Y.S., and Dong, J., 2015, "Drop-on-demand E-jet printing of continuous interconnects with AC-pulse modulation on highly insulating substrates," Journal of Manufacturing Systems, 37, pp. 505-510.

[10] Mishra, S., Barton, K. L., Alleyne, A. G., Ferreira, P. M., and Rogers, J. A., 2010, "High-speed and drop-on-demand printing with a pulsed electrohydrodynamic jet," Journal of Micromechanics and Microengineering, 20(9), pp. 095026.

[11] Phung, T. H., Kim, S., and Kwon, K.S., 2017, "A high speed electrohydrodynamic (EHD) jet printing method for line printing," Journal of Micromechanics and Microengineering, 27(9), pp. 095003.

[12] Yu, M., Ahn, K. H., and Lee, S. J., 2016, "Design optimization of ink in electrohydrodynamic jet printing: Effect of viscoelasticity on the formation of Taylor cone jet," Materials & Design, 89, pp. 109-115.

[13] Han, Y., Wei, C., and Dong, J., 2015, "Droplet formation and settlement of phase-change ink in high resolution electrohydrodynamic (EHD) 3D printing," Journal of Manufacturing Processes, 20, pp. 485-491.

[14] Shin, K.Y., Lee, S.H., and Oh, J. H., 2011, "Solvent and substrate effects on inkjet-printed dots and lines of silver nanoparticle colloids," Journal of Micromechanics and Microengineering, 21(4), pp. 045012.

[15] Gardner, M. R., Lewis, A., Park, J., McElroy, A. B., Estrada, A. D., Fish, S., Beaman, J. J., and Milner, T. E., 2018, "In situ process monitoring in selective laser sintering using optical coherence tomography," Optical Engineering, 57(4), p. 041407.

[16] Grasso, M., Laguzza, V., Semeraro, Q., and Colosimo, B. M., 2017, "In-process monitoring of selective laser melting: spatial detection of defects via image data analysis," Journal of Manufacturing Science and Engineering, 139(5), p. 051001.

[17] Wang, T., Kwok, T.H., Zhou, C. and Vader, S., 2018, “In-situ droplet inspection and closed-loop control system using machine learning for liquid metal jet printing,” Journal of Manufacturing Systems, 47, pp. 83-92.

[18] Imani, F., Yao, B., Chen, R., Rao, P., and Yang, H., "Fractal pattern recognition of image profiles for manufacturing process monitoring and control," Proc. ASME 2018 13th International Manufacturing Science and Engineering Conference, American Society of Mechanical Engineers, pp. V003T002A003.

[19] Wang, T., Kwok, T.-H., and Zhou, C., 2017, "In-situ droplet inspection and control system for liquid metal jet 3D printing process," Procedia Manufacturing, 10, pp. 968-981.

[20] Liu, C., Law, A.C.C., Roberson, D. and Kong, Z.J., 2019, "Image analysis-based closed loop quality control for additive manufacturing with fused filament fabrication," Journal of Manufacturing Systems, 51, pp.75-86.

[21] Singh, R., Zhang, X., Chen, Y., Zheng, J., and Qin, H., 2018, "In-situ real-time characterization of micro-filaments for electrohydrodynamic ink-jet printing using machine vision," Procedia Manufacturing, 17, pp. 45-52.

[22] Kam, K.M., Zeng, L., Zhou, Q., Tran, R. and Yang, J., 2013, "On assessing spatial uniformity of particle distributions in quality control of manufacturing processes," Journal of Manufacturing Systems, 32(1), pp.154-166.

[23] Kwon, K.S., and Lee, D.Y., 2013, "Investigation of pulse voltage shape effects on electrohydrodynamic jets using a vision measurement technique," Journal of micromechanics and microengineering, 23(6), pp. 065018.

[24] Nemoto, S., 1989, "Waist shift of a Gaussian beam by a dielectric plate," Applied optics, 28(9), pp. 1643-1647.

[25] Miller, D. A., 1991, "Huygens's wave propagation principle corrected," Optics letters, 16(18), pp. 1370-1372.

[26] Kirchhoff, G., 1883, "Zur theorie der lichtstrahlen," Annalen der Physik, 254(4), pp. 663-695.

[27] Green, G., 1828, An essay on the application of mathematical analysis to the theories of electricity and magnetism, Wezäta-Melins Aktiebolag.

[28] Born, M., and Wolf, E., 2013, Principles of optics: electromagnetic theory of propagation, interference and diffraction of light, Elsevier: Chapter 8.

[29] Jenkins, F. A., and White, H. E., 1958, "Fundamentals of optics," American Journal of Physics, 26(4), pp. 272-272.

[30] Cooley, J. W., and Tukey, J. W., 1965, "An algorithm for the machine calculation of complex Fourier series," Mathematics of computation, 19(90), pp. 297-301.

[31] Shannon, C. E., 1998, "Communication in the presence of noise," Proceedings of the IEEE, 86(2), pp. 447-457.

[32] Coppola, G., Ferraro, P., Iodice, M., De Nicola, S., Finizio, A., and Grilli, S., 2004, "A digital holographic microscope for complete characterization of microelectromechanical systems," Measurement Science and Technology, 15(3), pp. 529.

[33] Bradley, D., and Roth, G., 2007, "Adaptive thresholding using the integral image," Journal of graphics tools, 12(2), pp. 13-21.

[34] Atherton, T. J., and Kerbyson, D. J., 1999, "Size invariant circle detection," Image and Vision computing, 17(11), pp. 795-803.

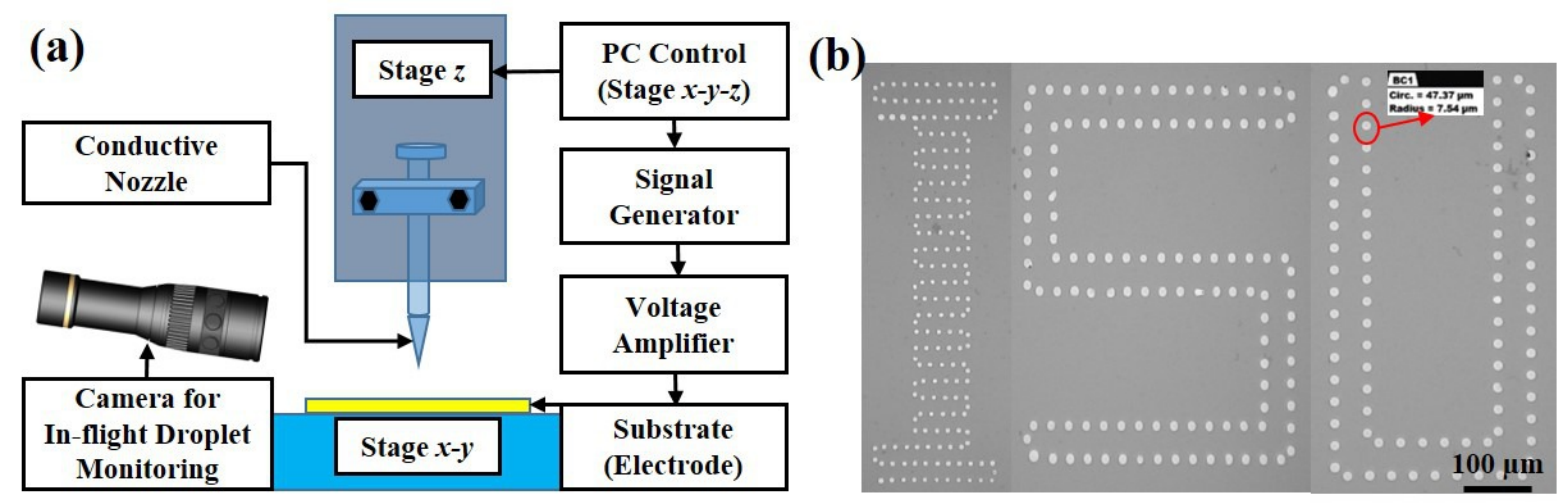
(a)
Stage z
PC Control
(Stage x-y-z)
Conductive
Nozzle
Signal
Generator
Voltage
Amplifier
Camera for
In-flight Droplet
Monitoring
Stage x-y
Substrate
(Electrode)
(b)
BC1
Circ. = 47.37 µm
Radius = 7.54 µm
100 µm

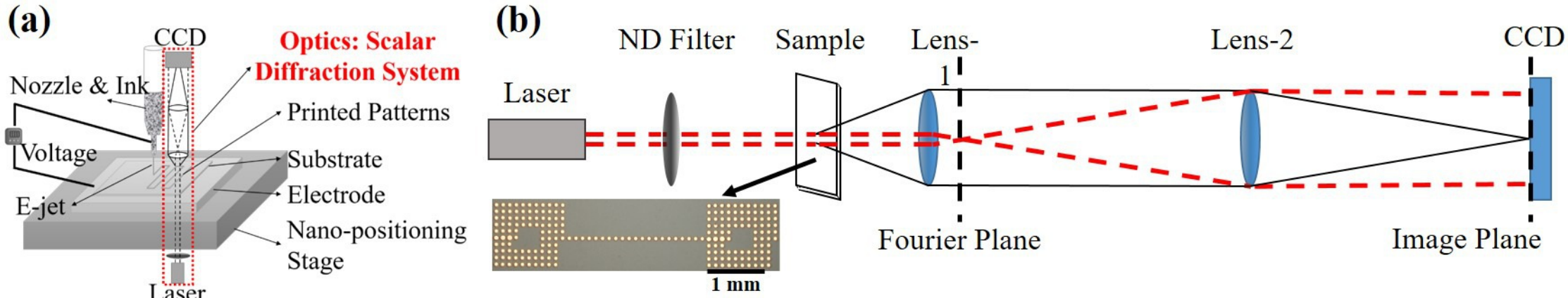
(a)
CCD
Optics: Scalar
Diffraction System
Nozzle & Ink
Printed Patterns
Voltage
Substrate
E-jet
Electrode
Nano-positioning
Stage
Laser
(b)
ND Filter
Sample
Lens-
1
Lens-2
CCD
Laser
Fourier Plane
Image Plane
1 mm

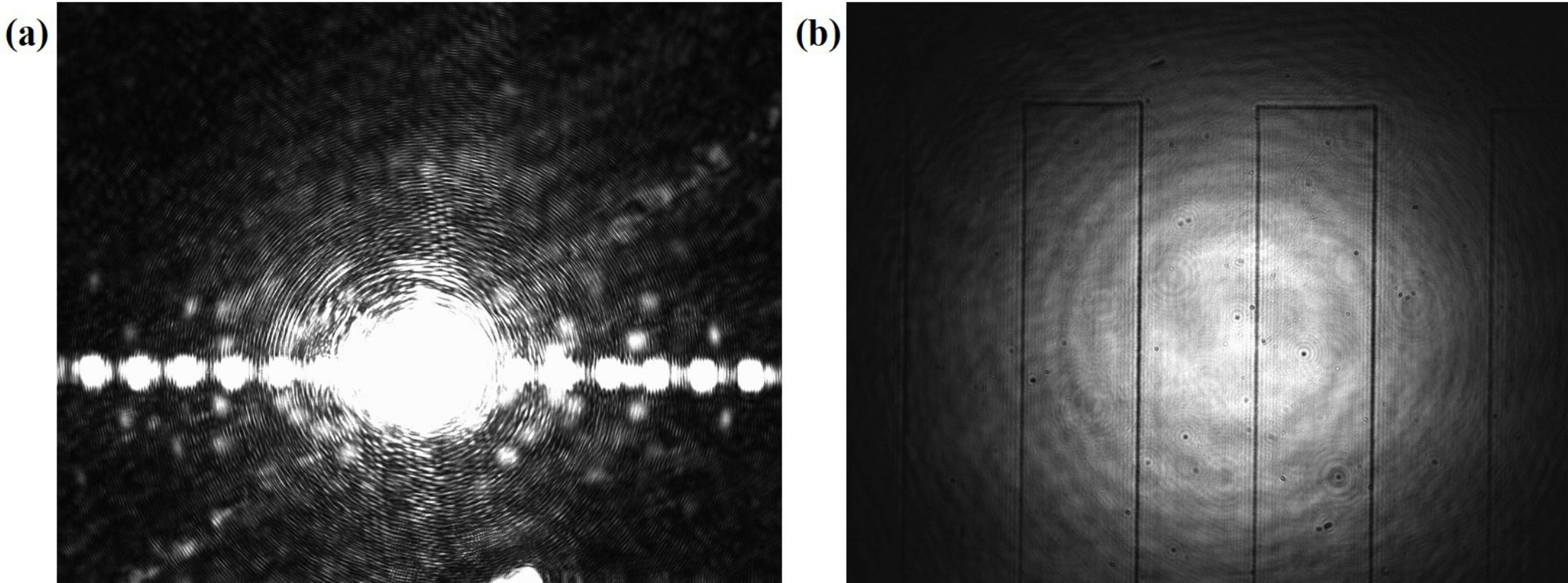
(a)
(b)

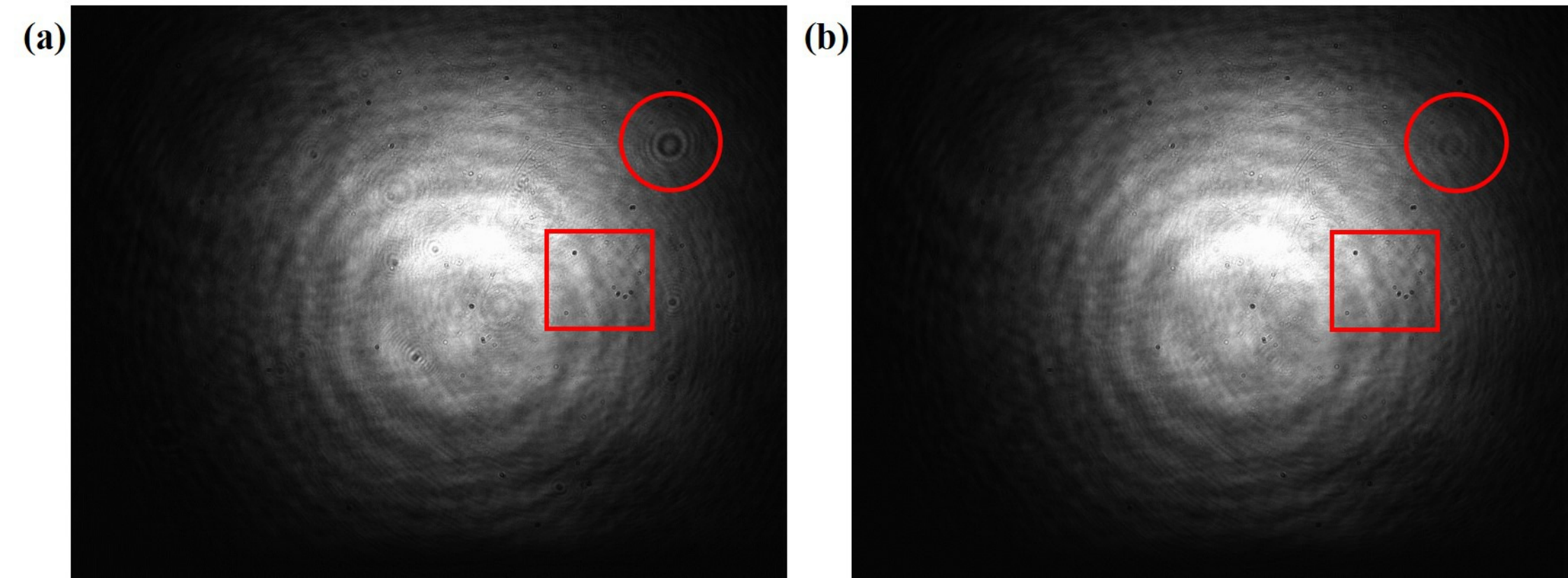
(a)
(b)

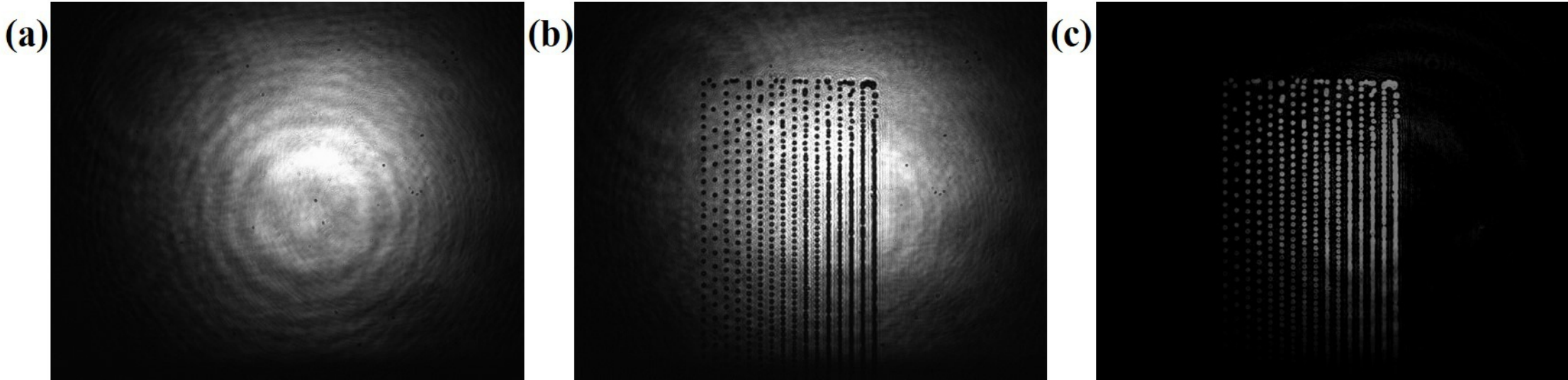
(a)
(b)
(c)

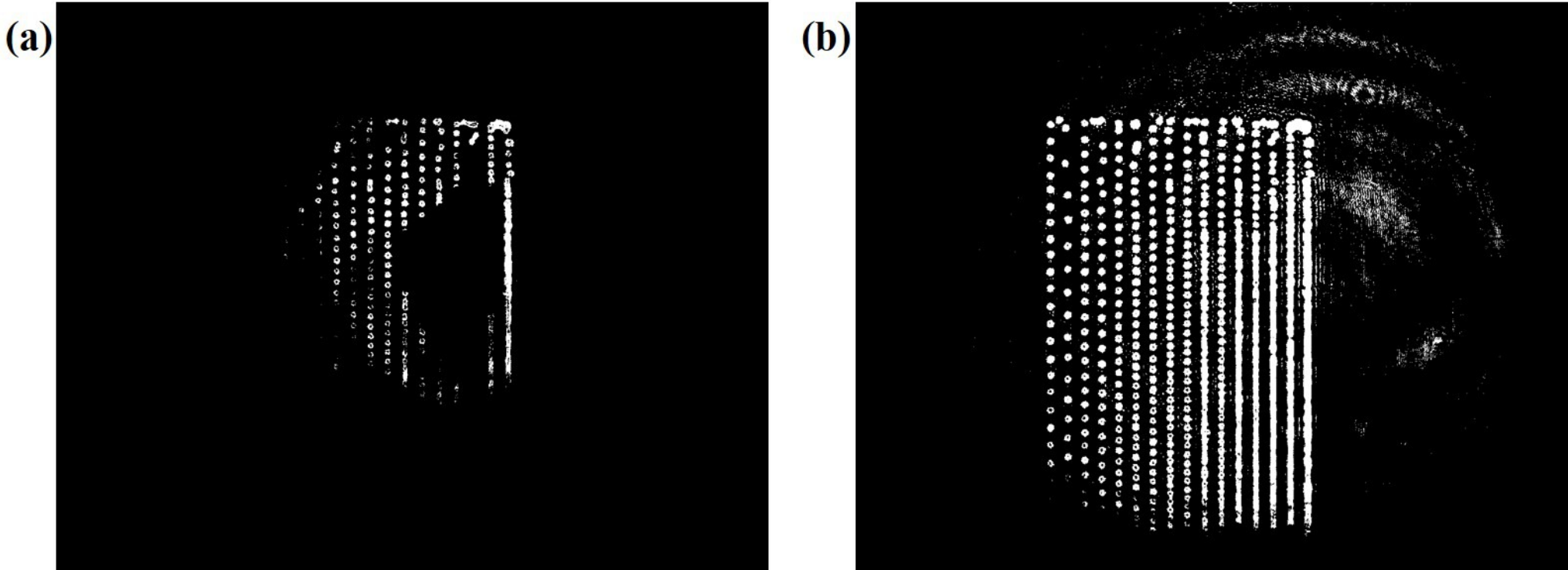
(a)
(b)

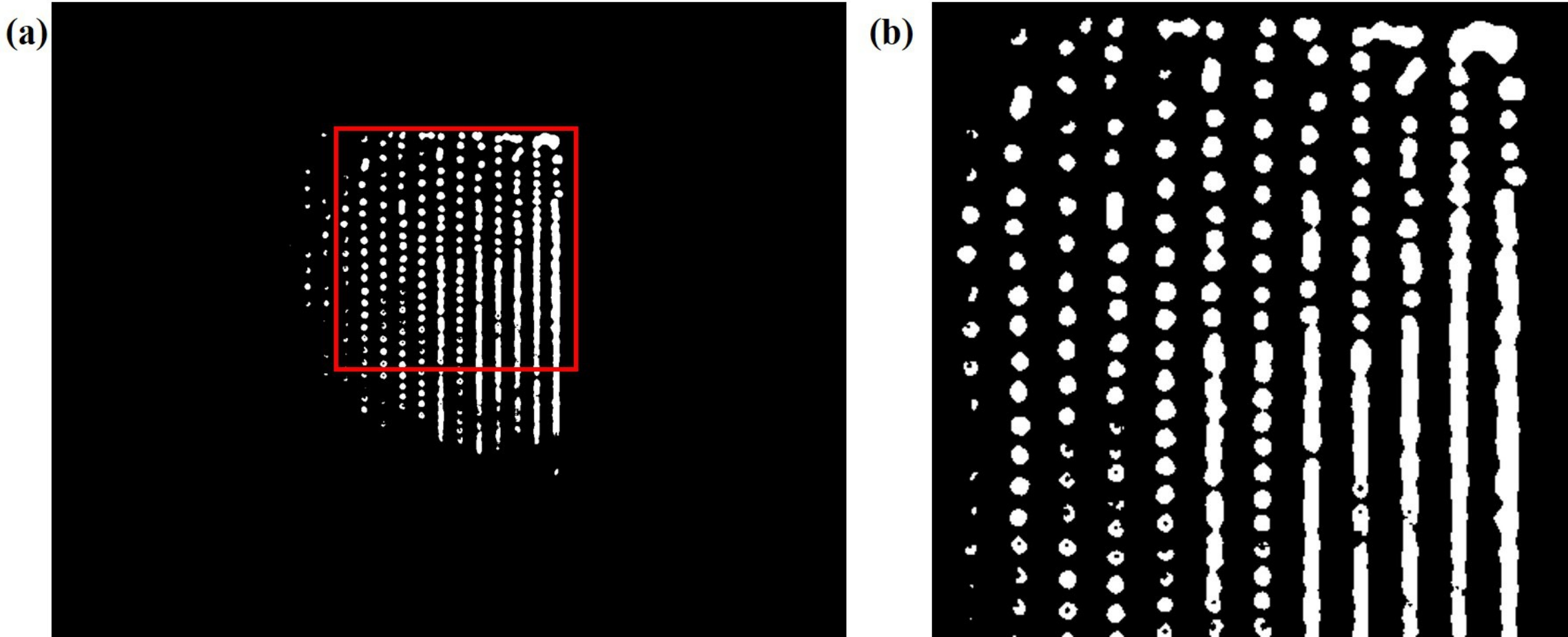
(a)
(b)

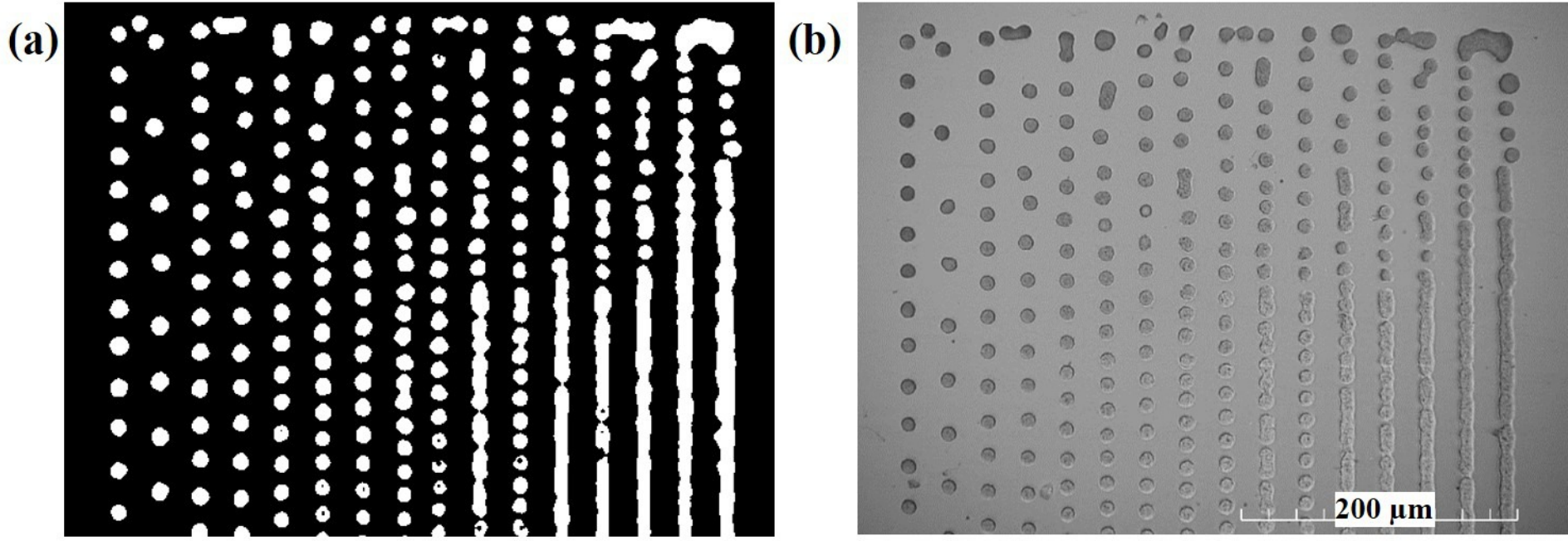
(a)
(b)
200 µm

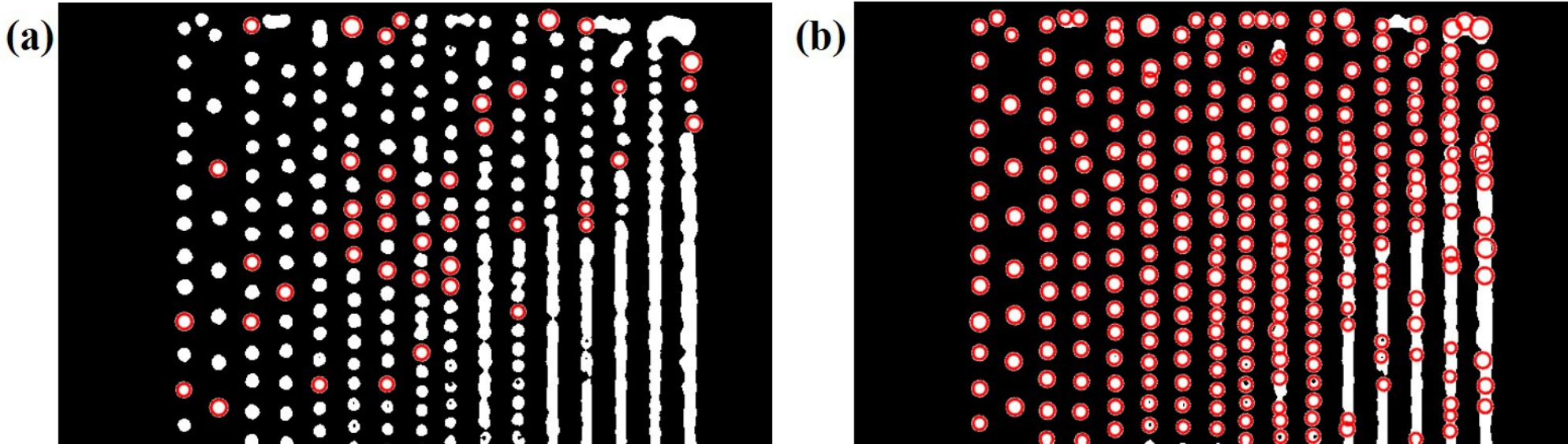
(a)
(b)

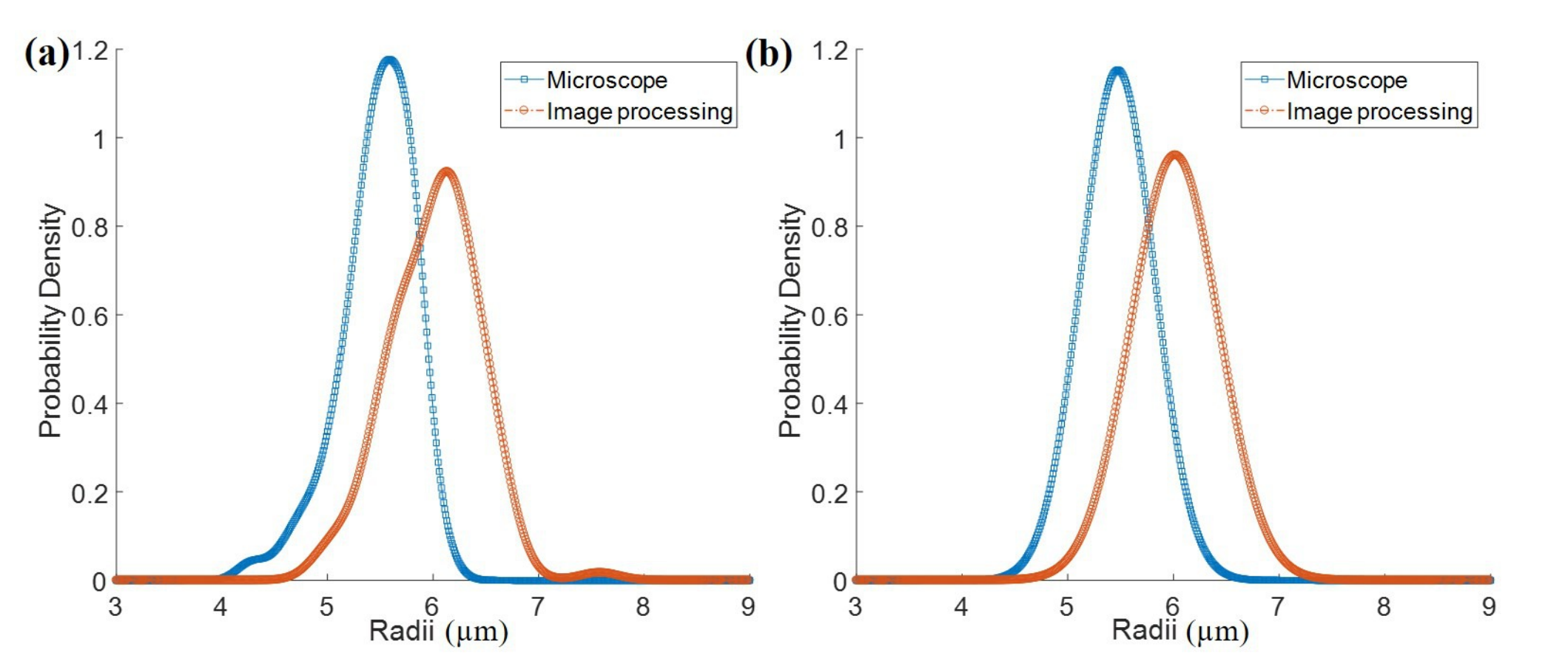
(a)
(b)
Microscope
Image processing
Probability Density
Radii (μm)
0
0.2
0.4
0.6
0.8
1
1.2
3
4
5
6
7
8
9

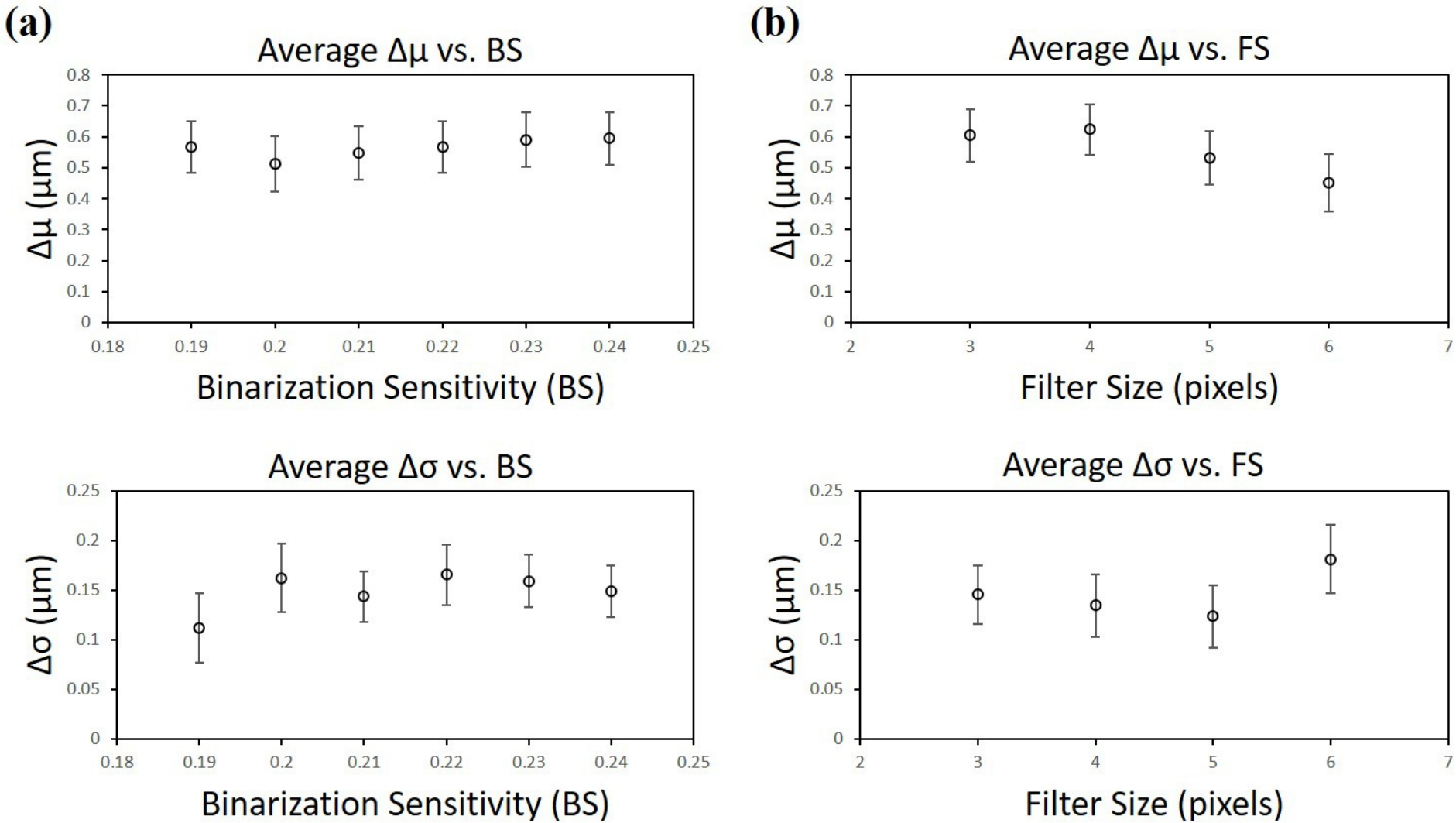
(a)
Average Δμ vs. BS
Δμ (μm)
0.8
0.7
0.6
0.5
0.4
0.3
0.2
0.1
0
0.18
0.19
0.2
0.21
0.22
0.23
0.24
0.25
Binarization Sensitivity (BS)
(b)
Average Δμ vs. FS
Δμ (μm)
2
3
4
5
6
7
Filter Size (pixels)
Average Δσ vs. BS
Δσ (μm)
0.25
0.2
0.15
0.1
0.05
0
Binarization Sensitivity (BS)
Average Δσ vs. FS
Filter Size (pixels)